

Narrow-Band Clutter Mitigation in Spectral Polarimetric Weather Radar

Yin, Jiapeng; Unal, Christine; Russchenberg, Herman

DOI

[10.1109/TGRS.2017.2696263](https://doi.org/10.1109/TGRS.2017.2696263)

Publication date

2017

Document Version

Final published version

Published in

IEEE Transactions on Geoscience and Remote Sensing

Citation (APA)

Yin, J., Unal, C., & Russchenberg, H. (2017). Narrow-Band Clutter Mitigation in Spectral Polarimetric Weather Radar. *IEEE Transactions on Geoscience and Remote Sensing*.
<https://doi.org/10.1109/TGRS.2017.2696263>

Important note

To cite this publication, please use the final published version (if applicable).
Please check the document version above.

Copyright

Other than for strictly personal use, it is not permitted to download, forward or distribute the text or part of it, without the consent of the author(s) and/or copyright holder(s), unless the work is under an open content license such as Creative Commons.

Takedown policy

Please contact us and provide details if you believe this document breaches copyrights.
We will remove access to the work immediately and investigate your claim.

Narrow-Band Clutter Mitigation in Spectral Polarimetric Weather Radar

Jiapeng Yin, *Student Member, IEEE*, Christine M. H. Unal, and Herman W. J. Russchenberg

Abstract—In this paper, a new clutter suppression method, named the moving double spectral linear depolarization ratio (MDsLDR) filter, is put forward to mitigate narrow-band clutter in weather radars. The narrow-band clutter observed in the Doppler domain includes: 1) stationary clutter such as ground clutter and 2) nonstationary clutter such as artifacts caused by the radar system itself or external sources. These artifacts are difficult to remove, because they are not confined to specific azimuth and range bins. Based on the difference of the spectral-polarization feature and the spectral continuity of precipitation and clutter, the MDsLDR filter can remove ground clutter, artifacts, and noise. The performance of the newly proposed filter is assessed by data collected by the Doppler-polarimetric IRCTR Drizzle Radar. Three precipitation cases are considered in this paper: moderate/light precipitation, convective precipitation with hook-echo signature, and light precipitation with severe artifact contamination. Furthermore, the implementation of the MDsDLR filter requires relatively low computation complexity, so that the MDsLDR filter can be operated in real time.

Index Terms—Narrow-band clutter, nonstationary clutter, real-time clutter mitigation, spectral continuity, spectral-polarimetry.

I. INTRODUCTION

THE presence of clutter may lead to misdetection of weather echoes or introduce bias on weather radar observables, which has aroused extensive attention in radar meteorology [1]. The radar environment is so complicated that it contains different sources of clutter, such as ground clutter, insects and birds, radio frequency interference, radar artifacts, and so on. These clutters significantly affect both the quality of the measurement and the observation of precipitation areas. Hence, it is important to find a way to suppress all the unwanted echoes.

For ground clutter suppression, the conventional method is the narrow notch filter centered around 0 ms^{-1} [2], whose performance depends on the spectral width of ground clutter. However, the spectral width is variable because of the change of environment and observation conditions. Moreover, sometimes the radial velocities of precipitation and ground clutter will overlap, leading to the loss of the target signal. To cope with these problems, the Gaussian model adaptive processing (GMAP) is introduced in [3]. The adaptive ground clutter suppression filter can recursively interpolate over the

removed clutter component to recover the overlapping precipitation signal. Moreover, GMAP can dynamically adjust the window type according to the calculated clutter to signal ratio (CSR). However, when GMAP is applied on noncontaminated gates, the reflectivity will be underestimated. Hence, it is necessary to detect the existence of clutter before the application of this suppression method. Combining with three discriminants—clutter phase alignment, texture of reflectivity, and spin—the clutter mitigation decision is proposed to identify the nonmeteorological echo [4], [5] in real time. Associating the GMAP with CMD, it results in significant improvements in ground clutter suppression on WSR-88D [6]. Nevertheless, there will be some signal loss due to the false detections along zero isodop by using the CMD technique. Additionally, there is also the problem of spatial irregularities in data fields with such combination.

Similar to CMD, a spectrum clutter identification (SCI), combining both the power and phase in the spectral domain, uses a Bayesian classifier to detect ground clutter mixed with weather signals [7]. The performance of SCI is better than CMD mostly in the low CSR. Likewise, the spectrum-time estimation and processing (STEP) algorithm integrates SCI, bi-Gaussian clutter filtering, and multilag moment estimation to fulfill clutter identification, clutter filtering, and noise reduction, respectively [8]. The STEP algorithm requires large computational resources, and further optimization should be conducted to implement in real time.

Recently developed clutter environment analysis using adaptive processing (CLEAN-AP) [9] is based on the phase of the autocorrelation spectral density. Compared with the combination of CMD and GMAP, CLEAN-AP uses both magnitude and phase for improved notch width determination that results in smaller biases, and it has more clutter suppression and less variance of estimates [10]. However, while CLEAN-AP can deal with normal-propagation and anomalous-propagation clutter, it is not a mitigation technique for moving clutter such as, airplanes and cars.

The CMD technique mentioned previously is one of the fuzzy logic algorithms adopted in the clutter identification. Others include the hydrometeor classification algorithm [11]–[13] and nonmeteorological echoes recognition proposed in [14] and [15]. The fuzzy logic algorithms are mainly based on the dual-polarization measurements, which provide additional echo features for classification. However, its robustness and effectiveness cannot be guaranteed because of different radar configurations and variable weather conditions.

In addition to ground clutter, other types of clutter are also reported in many publications. The characteristics of birds and insects are presented in [16]–[19]. Besides, [20]

Manuscript received September 28, 2016; revised February 3, 2017 and April 7, 2017; accepted April 16, 2017. (*Corresponding author: Jiapeng Yin.*)

The authors are with the Department of Geoscience and Remote Sensing, Faculty of Civil Engineering and Geoscience, Delft University of Technology, 2628 CN Delft, The Netherlands (e-mail: j.yin@tudelft.nl; c.m.h.unal@tudelft.nl; h.w.j.russchenberg@tudelft.nl).

Color versions of one or more of the figures in this paper are available online at <http://ieeexplore.ieee.org>.

Digital Object Identifier 10.1109/TGRS.2017.2696263

0196-2892 © 2017 IEEE. Personal use is permitted, but republication/redistribution requires IEEE permission.

See http://www.ieee.org/publications_standards/publications/rights/index.html for more information.

demonstrates the effectiveness of the image processing techniques together with fuzzy logic to mitigate other clutter, such as sea and chaff clutter.

Apart from the clutter mentioned previously, artifacts also affect the application of weather radar data. The artifacts are caused by the radar system itself or external sources displaying in the radar plan position indicator (PPI). Most of the time, artifacts are speckles along the whole range bins in some azimuth directions in the PPI. Consequently, these speckles are not confined to some range bins, and further they are nonstationary when observed in the Doppler domain, making it impossible to mitigate them with the conventional clutter suppression methods. These artifacts not only affect the reflectivity, but also the Doppler and polarimetric measurements. For example, artifacts have influenced the display of the polarimetric X-band radar IRCTR Drizzle Radar (IDRA), since its installation in 2007. Also, the high-resolution X-band radar MESEWI, which is currently under development at the Delft University of Technology, suffers from the similar problem [21]. Additionally, the C-band meteorological radars of the European operational weather radar network (EUMETNET/OPERA Radar Network [22]) increasingly becoming infected with the radio local area network need effective and real-time artifact removal techniques [23]. The artifact signatures, such as dots, spokes, or stripes, manifesting on the radar images caused by wireless technology are well documented in [24].

To deal with the dilemma of narrow-band clutter, including stationary ground clutter and nonstationary artifacts, this paper puts forward a method named the moving double spectral linear depolarization ratio (MDsLDR) filter to keep almost all the precipitation while removing the artifacts, ground clutter, and noise. Based on the spectral-polarization property and the spectral continuity, the newly proposed clutter suppression method implements its filtering in the range-Doppler spectrogram (i.e., one ray in radar PPI). MDsLDR filter adopts moving window to remove the unwanted clutter, and then the mathematical morphology method [25] is applied to recover the removed precipitation. The ray by ray clutter mitigation technique can be used regardless of different Doppler velocity resolutions. Furthermore, MDsLDR is proven to be computationally efficient and can be applied in real time.

The structure of this paper is as follows. In Section II, the IDRA system, its standard clutter suppression processing, and its artifacts are introduced. The details of the newly proposed method are provided in Section III. In Section IV, the parameter setting, the detailed implementation, and performance analysis are discussed. Furthermore, the MDsLDR filter is applied using different Doppler velocity resolutions. Then, two more cases are used to further verify the effectiveness of this newly proposed method. Finally, some conclusions are drawn in Section VI.

II. RESEARCH WEATHER RADAR OBSERVATION

A. Data Collection

The horizontally scanning polarimetric X-band IDRA was installed in the Dutch meteorological observatory, Cabauw Experimental Site for Atmospheric Research,

TABLE I
IDRA SPECIFICATIONS. THE BOLDFACE INDICATES PARAMETERS USED FOR THE OPERATIONAL MODE

Radar type	Linear FM-CW
Polarization	Fully polarimetric
Center frequency (GHz)	9.475
Transmitted power (W)	1, 2, 5, 10, 20
Range resolution (m)	3, 6, 15, 30
Sweep time (μ s)	204.8, 409.6 , 8192.2, 1638.4, 3276.8
Frequency sweep (MHz)	5 , 10, 20, 50
Antenna beamwidth ($^\circ$)	1.8
Elevation angle ($^\circ$)	0.5

in 2007 [26], [27]. On top of the 213-m atmospheric measurement mast, IDRA is the second highest location in the surroundings. IDRA is a linear frequency-modulated continuous waveform (FM-CW) radar with the center frequency 9.475 GHz. Moreover, this compact X-band radar is a polarimetric Doppler radar whose spectral polarimetric information can significantly improve the performance of signal processing and data processing. Additionally, IDRA rotates horizontally at the speed of 1 round/min with the fixed elevation angle 0.5° . The specifications of this polarimetric X-band radar are shown in Table I. Note that sweep, which is the terminology for FM-CW radar, is equivalent to pulse for pulse radar.

This compact X-band radar can provide a higher resolution precipitation map compared with lower frequency radars, such as S-band and C-band radars. All the radar data recorded from April 2009 until now are freely accessible to the public on the website named 4TU.centre for Research Data [28]. These data provide a long-term observation to monitor the trends in precipitation change. The range resolution and the Doppler velocity resolution are 30 m and 3.8 cms^{-1} , respectively, in the standard processing.

B. Standard Clutter Suppression Processing

Currently, the standard clutter suppression processing of IDRA is carried out in the range-Doppler domain. It consists of a narrow notch filter centered around 0 ms^{-1} and the DsLDR filter [29]. Furthermore, a noise clipping technique is implemented. It keeps the Doppler bins related to a spectral reflectivity at least 3 dB above the Doppler noise level. Finally, isolated Doppler bins and Doppler spectra containing less than 2% of Doppler bins are discarded. The DsLDR filter is based on the different distributions of the spectral-polarimetric parameter—sLDR [30] of precipitation and clutter.

These spectral polarimetric parameters are defined as [29]

$$\begin{aligned} \text{sLDR}^{\text{hh}}(v, r) &= 10\log_{10} \left(\frac{|S_{\text{vh}}(v, r)|^2}{|S_{\text{hh}}(v, r)|^2} \right) \\ \text{sLDR}^{\text{vv}}(v, r) &= 10\log_{10} \left(\frac{|S_{\text{hv}}(v, r)|^2}{|S_{\text{vv}}(v, r)|^2} \right) \end{aligned} \quad (1)$$

where $S_{xy}(v, r)$ represents the complex range-Doppler spectrogram with a transmitted y polarization and a receiving x polarization, x and y being horizontal or vertical polarization. Further v and r values are the Doppler velocity and the range, respectively. The assumption on the reciprocity condition $S_{\text{vh}} = S_{\text{hv}}$ is applied, which is true in theory and should be verified by measurements. Currently, for IDRA, only S_{vh} is measured.

Combining simultaneous Doppler and polarimetric information, it can improve the understanding of the microstructure of precipitation [31]. On the one hand, the Doppler information indicates the moving behavior of the precipitation scatterers that are within the resolution volume but are moving with different velocities. The spectral width of precipitation is an important feature to discriminate from other targets. On the other hand, LDR, which is the ratio between the cross-polar power and the copolar one, is widely used to classify different hydrometeors because of its sensitivity to their shape and orientation [32]. Currently, some weather radar systems, such as IDRA and Polarimetric Doppler Radar (POLDIRAD) [33], and cloud radars [34]–[36] are capable of measuring LDR. Normally, for cloud and precipitation targets, the cross-polar signal level is typically only 10^{-2} - 10^{-3} of the copolar level (LDR is in the interval of $[-20, -30]$ dB). Additionally, LDR measurements are prone to contamination from noise and clutter, leading to the increase in its values. Hence, sLDR can be used to distinguish the precipitation from noise and clutter. As a single spectral polarimetric parameter, it has been shown in [29] that it was the most efficient in reducing different types of clutter.

DsLDR filter has been proposed for an atmospheric radar slantly or vertically profiling the troposphere, and its full discussion can be referred to [29]. For horizontally profiling weather radar, the technique has to be combined with another clutter suppression method. Its shortcoming lies in that the sLDR of precipitation and clutter overlap, making it impossible to thoroughly separate them. Moreover, it is not desirable that the narrow notch filter may suppress the precipitation whose radial velocity is around 0 ms^{-1} and the noise clipping may remove the light precipitation.

C. Artifact Analysis

The IDRA radar continuously scans the atmosphere, and its measurements are displayed in real time. Considering one radar measurement, which occurred at 02:00 UTC on July 1, 2011, and applying the standard clutter suppression filtering method, the raw PPI and resulting PPI are shown in Fig. 1(a) and (b). This technique can reduce ground clutter, noise, and part of the artifacts. However, the mitigation of artifacts is not sufficient, which may also conduct a relatively high false alarm in the radar PPI; in the standard processing, it may conduct to -7 dB. It means that the Doppler bins related to an sLDR larger than -7 dB are discarded.

Considering the raw range-Doppler spectrogram of Ray 68 shown in Fig. 1(c), some artifacts are along the whole range bins, and they are nonstationary and their Doppler velocities vary. Furthermore, Range bin 300 (e.g., 9 km) is taken and its Doppler spectrum is plotted as shown in Fig. 1(d). We can see that the intensity of the precipitation is weaker than the artifacts and ground clutter. After integrating the whole Doppler bins resulting in one reflectivity value, the true reflectivity of precipitation will be biased by the artifacts and ground clutter. Moreover, the artifacts and precipitation are extracted and their sLDR^{hh} and sLDR^{vv} values are calculated based on (1) as shown in Fig. 1(e). From Fig. 1(e), the sLDR distribution value of the precipitation indicated as the red line are $[-40$ dB,

12 dB], while these of the artifacts are $[30$ dB, 0 dB], it is thus impossible to remove the artifacts when the threshold shown as the black dashed line is set to -7 dB. Note that the sLDR distribution of the precipitation in this case is largely increased by the effect of the low signal to noise ratio (SNR). In fact, in the case of low SNR precipitation, the cross-polar signal, $S_{hv}(v, r)$ and $S_{vh}(v, r)$, is not measured anymore, and only noise is measured. It means that sLDR^{hh} and sLDR^{vv} become an estimate of noise to signal ratio.

The spectral width property of the clutter and precipitation provides a way to remove all these clutter. After the statistical analysis of ten cases (each case contains more than 140 rays) during the time period from 2011 to 2016, we come to the conclusion that the spectral width of artifacts is always 3–4 Doppler resolution bins (about 15 cm s^{-1}), while that of ground clutter is 11–13 Doppler resolution bins (about 50 cm s^{-1}). The ground clutter spectra after the DsLDR filter are not fully removed. The remaining ground clutter spectra are discontinuous because of the partial removal of ground clutter Doppler bins, which is desirable for the newly designed filter. As for the precipitation, its spectral width is generally large and the Doppler spectrum is continuous. However, after the DsLDR filter, some points inside the spectra will be missing. This is mainly attributed to the fact that the low SNR will lead to the increase of the sLDR^{hh} and sLDR^{vv} values. Fortunately, the missing part can be compensated by the mathematical morphology method, which will be explained later. The details of the newly proposed filter in narrow-band clutter mitigation are discussed in Section III.

III. FILTER DESCRIPTION

The spectral properties can be used to distinguish precipitation from the narrow-band clutter in weather radar. Precipitation tends to be continuous across several range and Doppler bins in the range-Doppler domain. As for the feature of ground clutter, it is always static and centered around 0 ms^{-1} Doppler bin. While the artifacts of IDRA radar, exhibiting a spectral width less than 5 Doppler bins, appear continuously along the range bins and have an unpredictable position in one range-Doppler spectrogram. Based on all these features, the MDsLDR filter is proposed to remove the narrow-band clutter in spectral polarimetric radar. The method is mainly divided into four steps as shown in Fig. 2. The newly proposed filter is based on the range-Doppler spectrogram, thus it is a ray-by-ray process for radar PPI.

Step 1: The DsLDR filter is applied on the chosen spectrogram. The mask $M^{\text{DsLDR}} \in \{0, 1\}$ that characterizes precipitation is expressed as

$$M^{\text{DsLDR}} = \begin{cases} 1, & \text{if } \text{sLDR}^{\text{hh}} < T_1, \text{ sLDR}^{\text{vv}} < T_1 \\ 0, & \text{otherwise} \end{cases} \quad (2)$$

where T_1 is the set threshold, which can be related in the function of the radar configuration and its environment. $M^{\text{DsLDR}} = 1$ represents the potential areas of precipitation. After the DsLDR filter, however, the majority of the radar artifacts remains. This is because their sLDR values are smaller than the threshold T_1 , which has been illustrated in

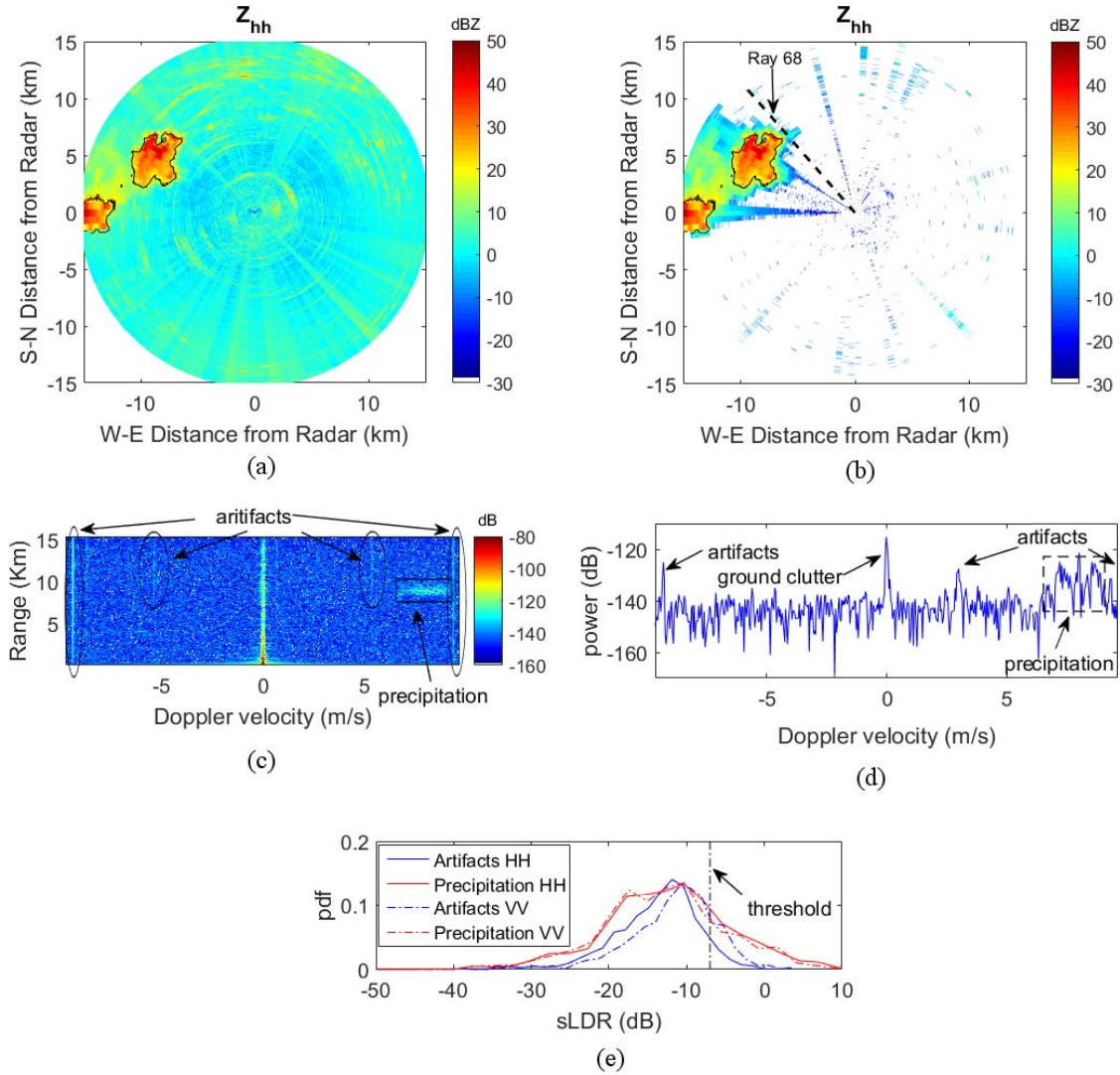


Fig. 1. IDRA artifacts observation. Data measured at 02:00 UTC on July 1, 2011. (a) Raw reflectivity PPI display. (b) Reflectivity PPI display after the standard processing. (c) Raw range-Doppler spectrogram of Ray 68. (d) Raw Doppler spectrum of Range bin 300 (e.g., 9 km). (e) Distributions of sLDR of artifacts and precipitation.

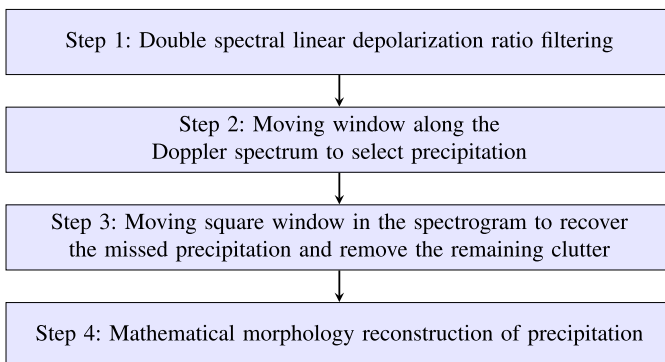


Fig. 2. Flowchart of the MDsLDR filter.

Section II. As for the ground clutter, their spectra become noncontinuous in the range-Doppler domain, which is favorable to Step 2. Additionally, some bins of the precipitation are eliminated, which is not

desirable but can be compensated by the moving 2-D window in Step 3 and the mathematical morphology method in Step 4.

Step 2: The moving window is applied along the Doppler domain to select precipitation. The $1 \times L$ Doppler moving window is set based on the analysis of the spectral width of the narrow-band clutter. Then the moving window is applied to the mask M^{DsLDR} obtained in Step 1. When the moving window traverses from the first bin to the last bin in one Doppler spectrum, the central bin as well as the $L/2$ bins before and after the chosen bin, altogether L bins, are considered as a whole. If there is 0 in any position of the moving window, the central bin is replaced with 0, otherwise maintained 1. With this process, a filtered mask M^{filtered} is obtained. However, it will lead to the loss of some “1” areas when they locate in the boundary of the precipitation, which will be compensated in the

next steps.

Step 3: The moving 2-D window is applied in the spectrogram to recover the missed precipitation and further eliminate the clutter. With the process of Step 2, almost all the narrow-band clutter is removed, but unfortunately, some precipitation, especially those locating in the boundaries, is also discarded. To further eliminate the very few remaining environment clutter and recover the filtered precipitation, a moving 2-D window sized $a \times b$ is applied to the filtered mask M^{filtered} . For each bin in the mask M^{filtered} , we apply the center of the moving window aligning to the chosen bin, and then we have $a \cdot b$ chosen elements $[M_1^{\text{filtered}}, M_2^{\text{filtered}}, \dots, M_{a \cdot b}^{\text{filtered}}]$. By summing them up and normalizing with the weight $1/a \cdot b$, we can get

$$K = \frac{1}{a \cdot b} \sum_{i=1}^{a \cdot b} M_i^{\text{filtered}}. \quad (3)$$

With the weight, the calculated K is in the interval $[0, 1]$. The comparison between K and the set threshold T_2 is made to decide whether the chosen bin is 1 or 0

$$M^{\text{MDsLDR}} = \begin{cases} 1, & \text{if } K > T_2 \\ 0, & \text{otherwise.} \end{cases} \quad (4)$$

With this moving 2-D window, it is possible to further remove the isolated bins in the filtered mask obtained in Step 2. Moreover, those points near the filtered “1” areas will be recovered. The selection of the length a and b of the moving window and the threshold T_2 will be discussed in Section IV where the technique is applied to real radar data.

Step 4: The mathematical morphology method is adopted to further reconstruct the precipitation. After the previous three steps, some points inside the precipitation area as well as the points in the boundaries may be filtered out. Then, the mathematical morphology, which is particularly useful for the analysis of binary images, can be used to recover them. The particular operator is the morphological closing whose function is removing small holes in the image processing. Closing is defined simply as a dilation followed by an erosion using the same structuring element for both operations. The details of the mathematical morphology method refer to [25]. The structuring element is set as the flat disk of radius r . The reason why the structuring element is set as the flat disk is that the precipitation areas are continuous in the range-Doppler spectrogram, and the flat disk is conducive to the smooth precipitation boundary recovery. The radius r should be properly set to recover sufficient precipitation bins.

IV. APPLICATION TO RADAR DATA

A. Parameter Setting

The parameters described in Section III are determined in this section for IDRA measurements. The threshold T_1 in Step 1 of the DsLDR filter applied to IDRA is -7 dB. The selection of T_1 is explained in [29]. Specifically, T_1 is selected considering clutter and precipitation removal percentage versus different thresholds. The threshold T_1 may differ for another radar (e.g., $T_1 = -5$ dB for transportable atmospheric radar [29]) because of different radar configurations and clutterers. For example, a vertically profiling radar is less affected by ground clutter than a horizontally profiling one.

As for the length of the Doppler moving window L in Step 2, it depends on the spectral width of the narrow-band clutter, and L corresponds to the largest Doppler spectral width observed for this clutter. For IDRA in the operational mode with 512 sweeps for the Doppler processing, $L = 5$ (about 20 cm s^{-1}).

In Step 3, with no loss of generality, the moving 2-D window can be squared with size $a = b$. Then, the choice of the side length SL of the moving square window as well as the threshold T_2 are important to recover the removed precipitation bins and eliminate the remaining clutter bins. On the one hand, the boundaries of precipitation in the range-Doppler domain will be removed in Step 2, so the threshold T_2 for the moving 2-D square window should be small to recover more marginal precipitation. On the other hand, there is some isolated clutter remaining in the range-Doppler spectrogram, which should be further suppressed otherwise it will bring in more surrounding clutter with Step 4. In other words, the threshold T_2 should be large enough to further mitigate the isolated clutter. The later factor is dominant because the marginal precipitation affects less the final reflectivity calculation.

Next, the selection of side length SL and threshold T_2 will be explored in detail. The reflectivity derived from the range-Doppler spectrogram is proportional to the power sum along the Doppler bins. Supposing for a given spectrogram, we have R range bins with precipitation, and then a parameter named average error reflectivity δZ_{hh} is defined as

$$\delta Z_{\text{hh}} = \frac{1}{R} \sum_{r=1}^R |Z_{\text{hh}}^{\text{true}}(r) - Z_{\text{hh}}^{\text{est}}(r)| \quad (5)$$

where $Z_{\text{hh}}^{\text{true}}(r)$ is the true reflectivity value in the r th range bin, and $Z_{\text{hh}}^{\text{est}}(r)$ is the filtered reflectivity value in the r th range bin. Based on the δZ_{hh} , a method named the average error reflectivity minimization can be used to select the side length SL and threshold T_2 .

Considering the spectrogram in Fig. 1(c) to calculate the $Z_{\text{hh}}(r)$ (r in the interval of $8.6\text{--}9.1$ km), the true $Z_{\text{hh}}^{\text{true}}(r)$ and the MDsLDR filtered $Z_{\text{hh}}^{\text{est}}(r)$ with $\text{SL} \in [3, 7]$ with a step 1 and $T_2 \in [0.1, 0.4]$ with a step 0.05 are calculated. Furthermore, the δZ_{hh} value is obtained and its contour map is shown in Fig. 3. Note that the sweep number is 512 here.

From Fig. 3, it is concluded that similar average error reflectivity values may be obtained for different combinations of SL and T_2 . Hence, one of these two parameters can be preset, and the other one can be selected based on the average

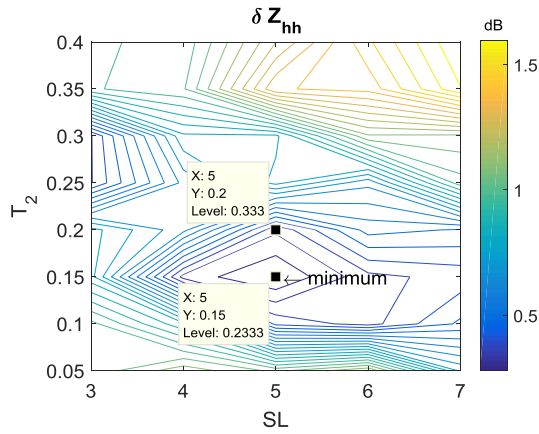


Fig. 3. Average error reflectivity δZ_{hh} calculation based on different side length SL values and threshold T_2 values.

error reflectivity minimization. L is used in Step 2 as the length of the moving window along the Doppler domain, while the selection of SL is the 2-D window to further mitigate the isolated clutter and recover the marginal precipitation. The 2-D window takes advantage of the continuity of precipitation in the range-Doppler domain. Thus, L and SL can be related to each other, and we set $L = SL$. From Fig. 3, with $SL = 5$ and $T_2 = 0.15$, we obtain the minimum $\delta Z_{hh} = 0.23$ dB, which is consistent with our analysis, namely presetting $SL = L$ and then exploring T_2 based on the average error reflectivity minimization. Note that such parameter selection may be optimal for the adopted spectrogram, and further validation should be implemented for other measurements. As discussed previously, T_2 should be relatively large to mitigate more isolated background clutter. Hence, we set $SL = 5$ and $T_2 = 0.2$ whose corresponding $\delta Z_{hh} = 0.33$ dB is the final average reflectivity error for the spectrogram at high Doppler resolution. Furthermore, ten cases (each case contains more than 140 rays) during the time from 2011 to 2016 are tested, and it verifies the effectiveness of the configuration of $SL = 5$ and $T_2 = 0.2$ for the operational mode. Some results are presented in Section V.

Finally, in Step 4, the radius of the flat disk can be set as $r = L$. The reason is easy to understand. The radius of this structuring element used here is to recover the excessive removal of precipitation, which is done in Step 2 with one moving window sized $1 \times L$. With $r = L$, it is expected that the recovered precipitation can fully compensate the precipitation boundaries.

To reiterate, the parameter selection in the MDsLDR filter is based on radar configuration and the clutter property, e.g., spectral width. Apart from that, the parameters in Step 3 are also chosen based on the radar data. Normally, for the situations with different sweep numbers, the parameter selection procedure in Step 3 should be applied.

B. Implementation and Performance Analysis

When the parameters are determined, the MDsLDR filter can be implemented according to the flowchart in Fig. 2. To better understand each step described in the block diagram, the corresponding spectrogram after each step is shown

in Fig. 4. From Fig. 4(a), the spectrogram after the DsLDR filter is not desirable, because there are radar artifacts as well as background noise and ground clutter remaining. In this case, the intensity of precipitation is so weak that it will be largely biased when Z_{hh} is calculated based on this result. Then, with the moving window in the Doppler domain, Fig. 4(b) shows that for all the artifacts, the majority of background noise and most of precipitation are mitigated. The precipitation removal is not favorable, which should be recovered later. In Fig. 4(c), with the moving 2-D window, the isolated noise is further reduced, and some precipitation is recovered. Finally, with the mathematical morphology reconstruction in Fig. 4(d), almost all the precipitation remains and all the artifacts, the noise, and the ground clutter are removed. From this spectrogram comparison, the newly proposed MDsLDR technique shows full artifacts, ground clutter, and noise suppression.

To further make a comparison between the DsLDR filter and the MDsLDR filter, the Doppler spectra of Range bin 300 after the DsLDR and the MDsLDR filtering are shown in Fig. 5(a). From Fig. 5(a), it is obvious that the MDsLDR filter has better clutter suppression performance than the DsLDR filter only. Additionally, the Doppler spectra of precipitation after the MDsLDR filter are continuous, and the DsLDR filtered ones have some missing data.

After having illustrated the effectiveness of the MDsLDR filter, it is necessary to quantitatively verify the performance of the technique. To quantify the results, the error reflectivity in the r th range bin $\Delta Z_{hh}(r)$ is defined as

$$\Delta Z_{hh}(r) = Z_{hh}^{\text{true}}(r) - Z_{hh}^{\text{est}}(r). \quad (6)$$

The error reflectivity $\Delta Z_{hh}(r)$ and the average error reflectivity δZ_{hh} defined in (5) are used to characterize the filter performance. The morphological closing operator is an essential step in the MDsLDR filter, which will also be studied here. The true reflectivity, the DsLDR filtered reflectivity, and the MDsLDR filtered reflectivity with and without the mathematical morphology process are shown in Fig. 5(b). Note that the “MDsLDR no MM” in the legend means the MDsLDR filter without the mathematical morphology process.

From Fig. 5(b), the mathematical morphology process plays an indispensable role in the precipitation recovery, especially for the precipitation boundaries. The maximum error reflectivity $\Delta Z_{hh}(r)$ and the average error reflectivity δZ_{hh} of the MDsLDR filter is 1.09 and 0.33 dB. While these errors between the MDsLDR filter without the mathematical morphology process and true reflectivity are 3.66 and 1.03 dB. The maximum $\Delta Z_{hh}(r)$ difference with and without the mathematical morphology process is as high as 2.57 dB. As for the DsLDR filtered reflectivity, its average error reflectivity is 1.63 dB, which is the worst among the three filters. Additionally, its reflectivity is always larger than the true reflectivity. The reason is the residual ground clutter and artifacts remaining because of the incomplete filtering as shown in Fig. 5(a). It can be concluded that the Z_{hh} value obtained from the MDsLDR filter with the mathematical morphology process is the best fit to the true Z_{hh} value. Note that the

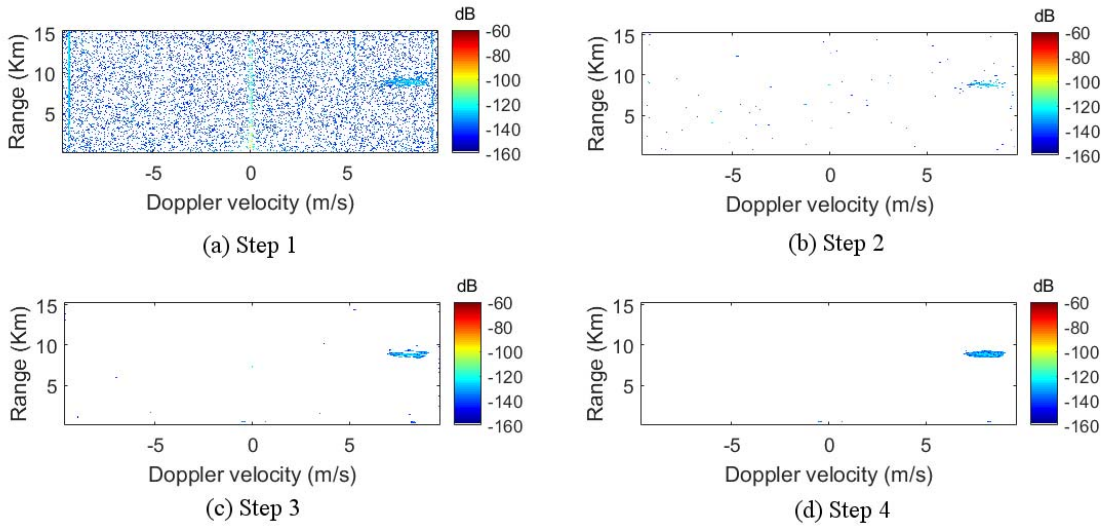


Fig. 4. Output range-Doppler spectrogram after each step of the flowchart. (a) Step 1. (b) Step 2. (c) Step 3. (d) Step 4.

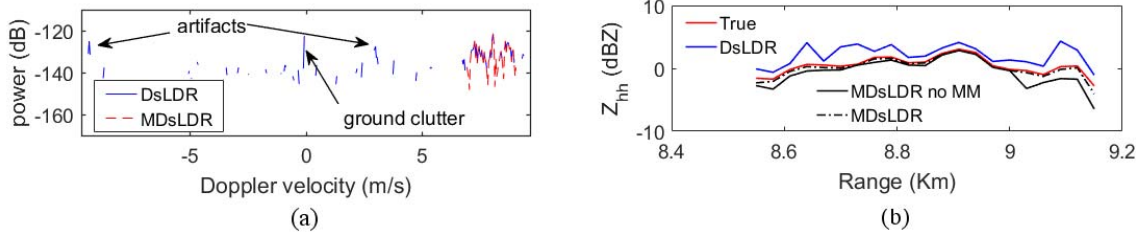


Fig. 5. Performance comparison between the DsLDR filter and the MDsLDR filter. (a) Filtered Doppler spectrum of Range bin 300. (b) Z_{hh} comparison.

true reflectivity is around 0 dBZ, corresponding to very light precipitation.

The above-mentioned analysis validates the good performance of the MDsLDR filter applied to the range-Doppler spectrogram. For the operational polarimetric radar, the filtered observables displaying in the PPI are required. Hence, by applying the MDsLDR filter to all the spectrograms in one PPI, we calculate the reflectivity Z_{hh} , differential reflectivity Z_{dr} , and LDR as shown in Fig. 6(b), (d), and (f), respectively. Making a comparison with the standard processing results based on the DsLDR filter as shown in Fig. 6(a), (c), and (e), almost all the precipitation remains while the artifacts are suppressed with the MDsLDR filter. Furthermore, the scatter plot of the MDsLDR filtered Z_{hh} and the Z_{hh} after the standard processing is shown in Fig. 6(g). It indicates that the artifacts have a larger impact on Z_{hh} smaller than 0 dBZ, which usually corresponds to light precipitation or drizzle.

To further quantify the filtering performance of the MDsLDR filter in the PPI, the clutter suppression ratio Z_{hh}^{CSR} expressed in *dB* is defined as

$$Z_{hh}^{CSR} = Z_{hh}^{original} - Z_{hh}^{MDsLDR} \quad (7)$$

where $Z_{hh}^{original}$ is the original reflectivity without any filtering, and Z_{hh}^{MDsLDR} is the reflectivity after the MDsLDR filtering. The histogram of the clutter suppression ratio Z_{hh}^{CSR} is shown in Fig. 6(h). The maximum clutter suppression ratio is as high

as 43.0 dB for this adopted case occurred at 02:00 UTC on July 1, 2011.

Note that the polarimetric features of artifacts can be low Z_{hh} (around 0 dBZ), large Z_{dr} (around 1 dB) and low LDR (around -15 dB), which are typical precipitation features. These comparisons verify the effectiveness of the proposed filter for artifact mitigation especially in the presence of light precipitation. It is foreseeable that the MDsLDR filter improves the data quality of polarimetric weather radar and makes the measured data available for further application. However, other precipitation cases have to be considered for an independent evaluation, which will be shown in Section V.

C. Impact of the Doppler Resolution

The current operational weather radars tend to scan faster to update the atmospheric changes in shorter time. This means a shorter dwell time for the Doppler processing. This section will further verify the effectiveness of the MDsLDR filter regarding different Doppler resolutions.

Using the same data measured at 02:00 UTC on July 1, 2011, we set the sweep number to 512, 256, 128, and 64 to explore the performance of the MDsLDR filter. Since the total sweep number of one PPI is fixed, to get the same data for comparison, the increasing multiple of the ray number is the same with the decreasing multiple of sweep number in the data selection. As for the selection

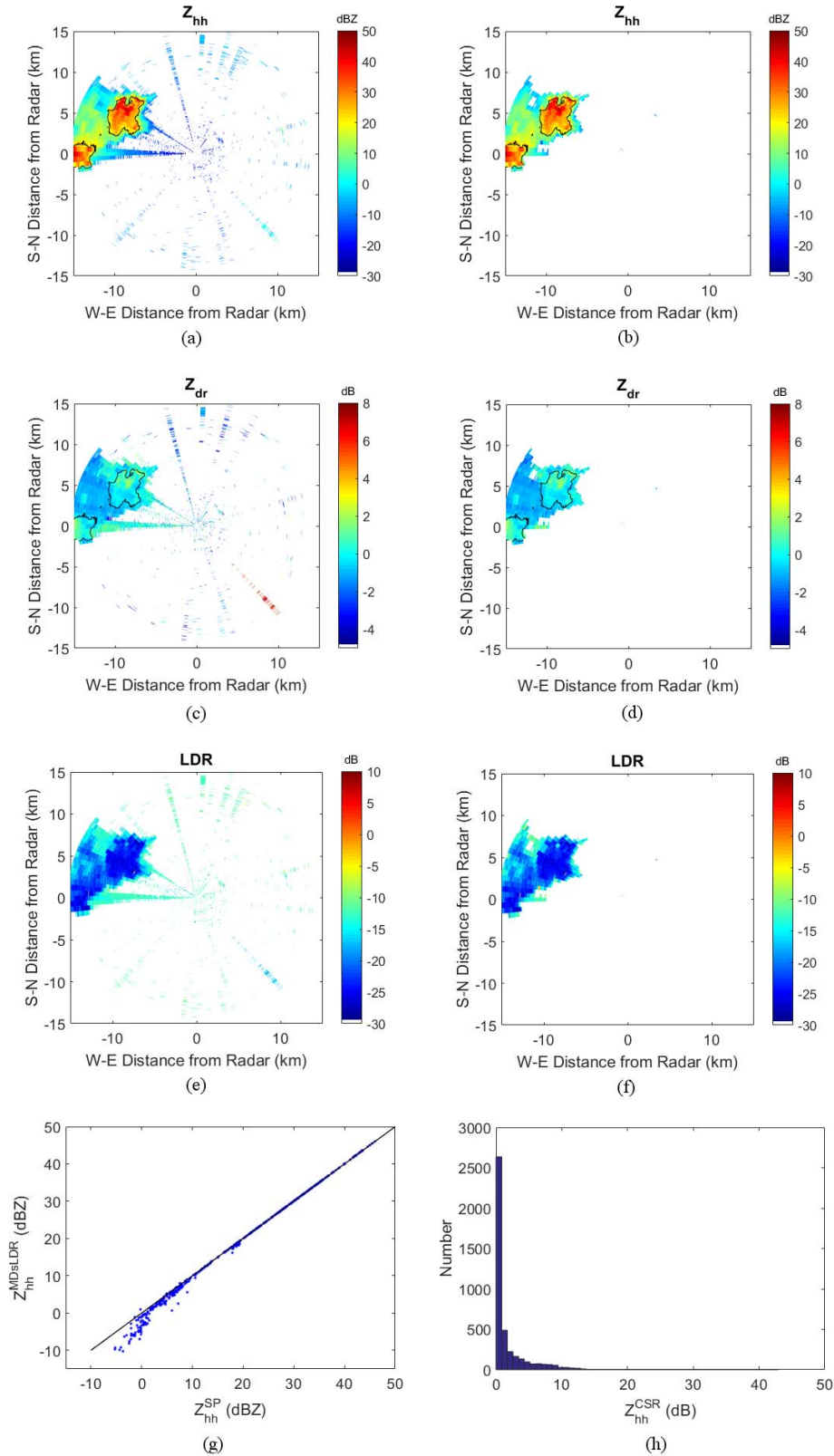


Fig. 6. PPI comparison between the standard processing and the MDsLDR filter. Data measured at 02:00 UTC on July 1, 2011. (a) Z_{hh} after the standard processing. (b) Z_{hh} after the MDsLDR filter. (c) Z_{dr} after the standard processing. (d) Z_{dr} after the MDsLDR filter. (e) LDR after the standard processing. (f) LDR after the MDsLDR filter. (g) Z_{hh} comparison between the MDsLDR filter and the standard processing. (h) Clutter suppression ratio distribution.

of L , it is obtained by the observation of spectral width of the narrow-band clutter in the range-Doppler spectrogram. Finally, as discussed in Section IV-A, by setting $SL = L$, the T_2 is determined based on the average error reflectivity

minimization. The results of parameter selection are shown in Table II.

With the parameter selection in Table II, another measurement should be used to verify the filter effectiveness.

TABLE II
MDsLDR PARAMETER SELECTION FOR DIFFERENT DOPPLER RESOLUTIONS

Sweep number	Doppler velocity resolution (m/s)	Ray No	L	T_2	SL
512	3.8×10^{-2}	68	5	0.2	5
256	7.5×10^{-2}	135	4	0.2	4
128	1.5×10^{-1}	269	3	0.3	3
64	3.0×10^{-1}	537	3	0.35	3

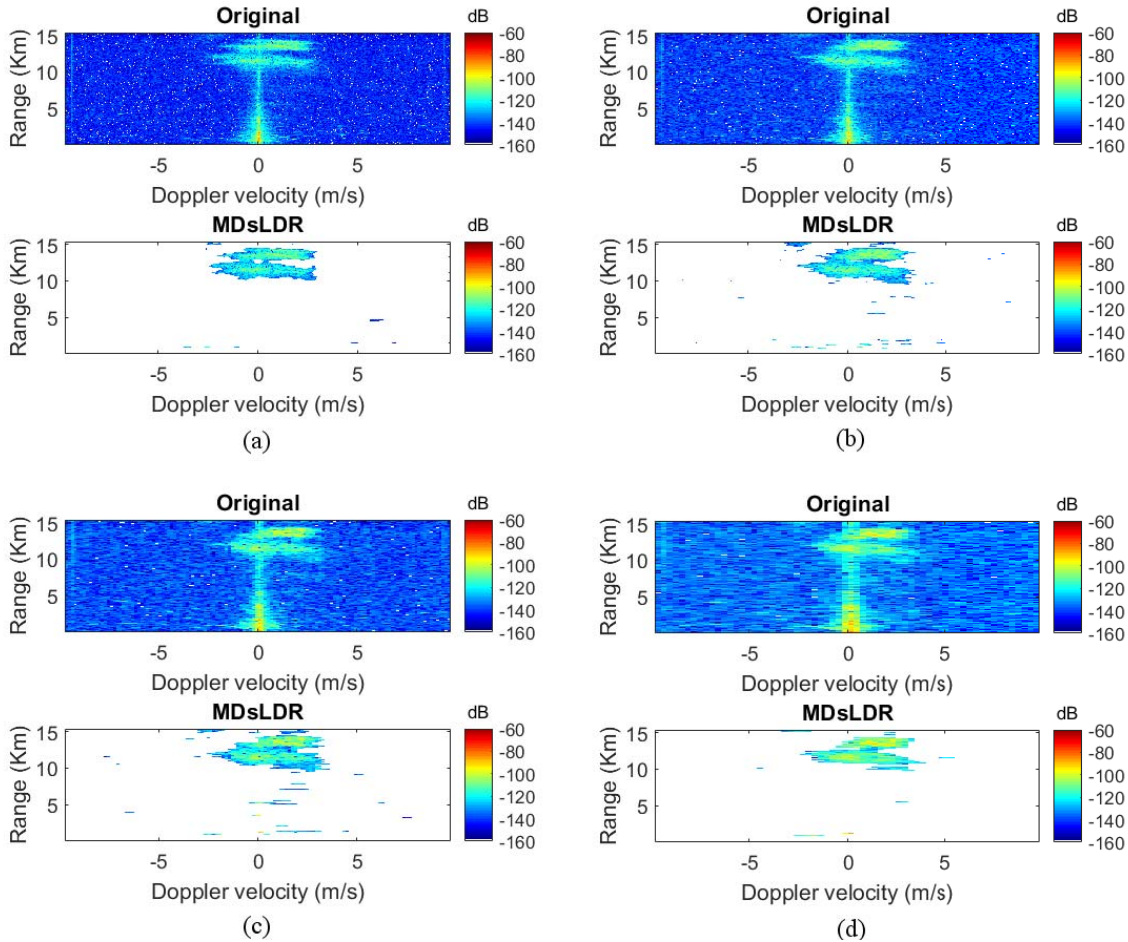


Fig. 7. MDsLDR filter applied to radar data with different Doppler resolutions. (a) Sweep number 512. (b) Sweep number 256. (c) Sweep number 128. (d) Sweep number 64.

Data measured at 12:00 UTC on July 1, 2011 are selected, and Rays 142, 284, 568, and 1136 are considered for different Doppler velocity resolutions. The results are shown in Fig. 7. From Fig. 7(a)–(d), we can observe that the MDsLDR filter can preserve almost the precipitation while removing all the clutter. These results further verify that MDsLDR filter can be adopted for different Doppler velocity resolutions. Note that, in this case, when the ground clutter overlaps with precipitation, MDsLDR cannot mitigate the ground clutter, and other technique should be used to resolve this situation.

V. OTHER CASE STUDIES

A. Apply to Severe-Storm Case

To assess the MDsLDR filter, a case of a severe storm is illustrated here. The data measurement occurred at 14:45 UTC on January 3, 2012 when a cold-season organized storm

crossed The Netherlands from the northwest to the southeast. The IDRA radar observed reflectivity signatures, such as hook echo and weak echo region, which are associated with supercell vortices. A successful clutter suppression method should retain this important reflectivity signature while mitigating the unwanted clutter.

Fig. 8(a) and (b) is the PPI after the standard processing and the MDsLDR filter, respectively. From the comparison of them, it seems that they are almost the same. In particular, the important reflectivity signature—hook echo remains. This is consistent with the above-mentioned analysis—the artifacts affect less large reflectivity zone. The only difference is that some areas in the PPI are free of echoes with the MDsLDR filter. In this case, it is difficult to judge which filter results in better clutter suppression performance. Hence, an inspection of the spectrogram is necessary, and Ray 45 is used here.

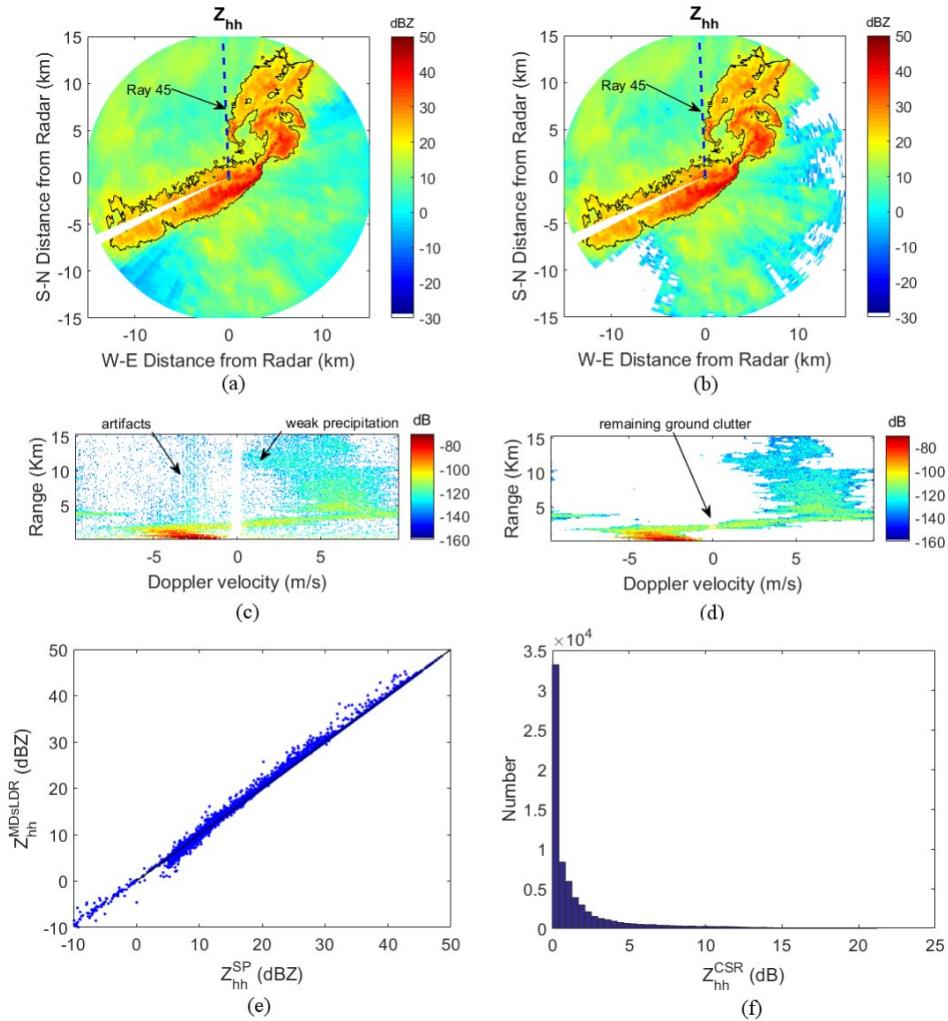


Fig. 8. Severe-storm case. Data measured at 14:45 UTC on January 3, 2012. (a) Z_{hh} after the standard processing. (b) Z_{hh} after the MDsLDR filter. (c) Spectrogram of Ray 45 after the standard processing. (d) Spectrogram of Ray 45 after the MDsLDR filter. (e) Z_{hh} comparison between the MDsLDR filter and the standard processing. (f) Clutter suppression ratio distribution.

Compared with the MDsLDR filtered spectrogram as shown in Fig. 8(d), the standard processing filtered spectrogram in Fig. 8(c) has an inferior performance. Specifically, after the standard processing, some of the artifacts remain, and some light precipitation is also reduced by the fixed notch filter. While for the MDsLDR filter, all the artifacts and the ground clutter, which is not overlapping with precipitation, are discarded. Additionally, almost all the areas with precipitation in the range-Doppler domain are maintained.

Finally, the scatter plot of the MDsLDR filtered Z_{hh} and the Z_{hh} after the standard processing is shown in Fig. 8(e). Normally, the standard processing filtered Z_{hh} has a larger value than the MDsLDR filtered one because of the residual artifacts. However, in this case where ground clutter and precipitation overlap for some range bins, the Z_{hh} after the standard processing has a smaller value. This is because the notch filter adopted in the standard processing will remove all the ground clutter while the MDsLDR filter will retain the ground clutter overlapping with precipitation. This is shown in Fig. 8(c) and (d). Then, it is concluded that the MDsLDR

filter cannot resolve the situation of ground clutter overlapping with precipitation, which means that another technique should be combined. The histogram of the clutter suppression ratio is shown in Fig. 8(f). Note that the maximum clutter suppression ratio, in this case, is 21.2 dB.

B. Apply to Severe-Artifacts Case

To further verify the performance of the newly proposed method in narrow-band clutter removal, another case with severe artifacts is used here. The case occurred at 12:00 UTC on January 15, 2016. The results of Z_{hh} and Z_{dr} after the standard processing and the MDsLDR filter are shown in Fig. 9. Apart from these PPI displays, a further check of Ray 69 and the scatter plot of Z_{hh} between the two techniques are also included.

From Fig. 9(a) and (c), we can see that artifacts severely contaminate the reflectivity Z_{hh} and the differential reflectivity Z_{dr} . While after the MDsLDR filtering, a better artifact suppression can be achieved as shown in Fig. 9(b) and (d). However, for the differential reflectivity Z_{dr} , the azimuthal discontinuities are still present. They are not the result of

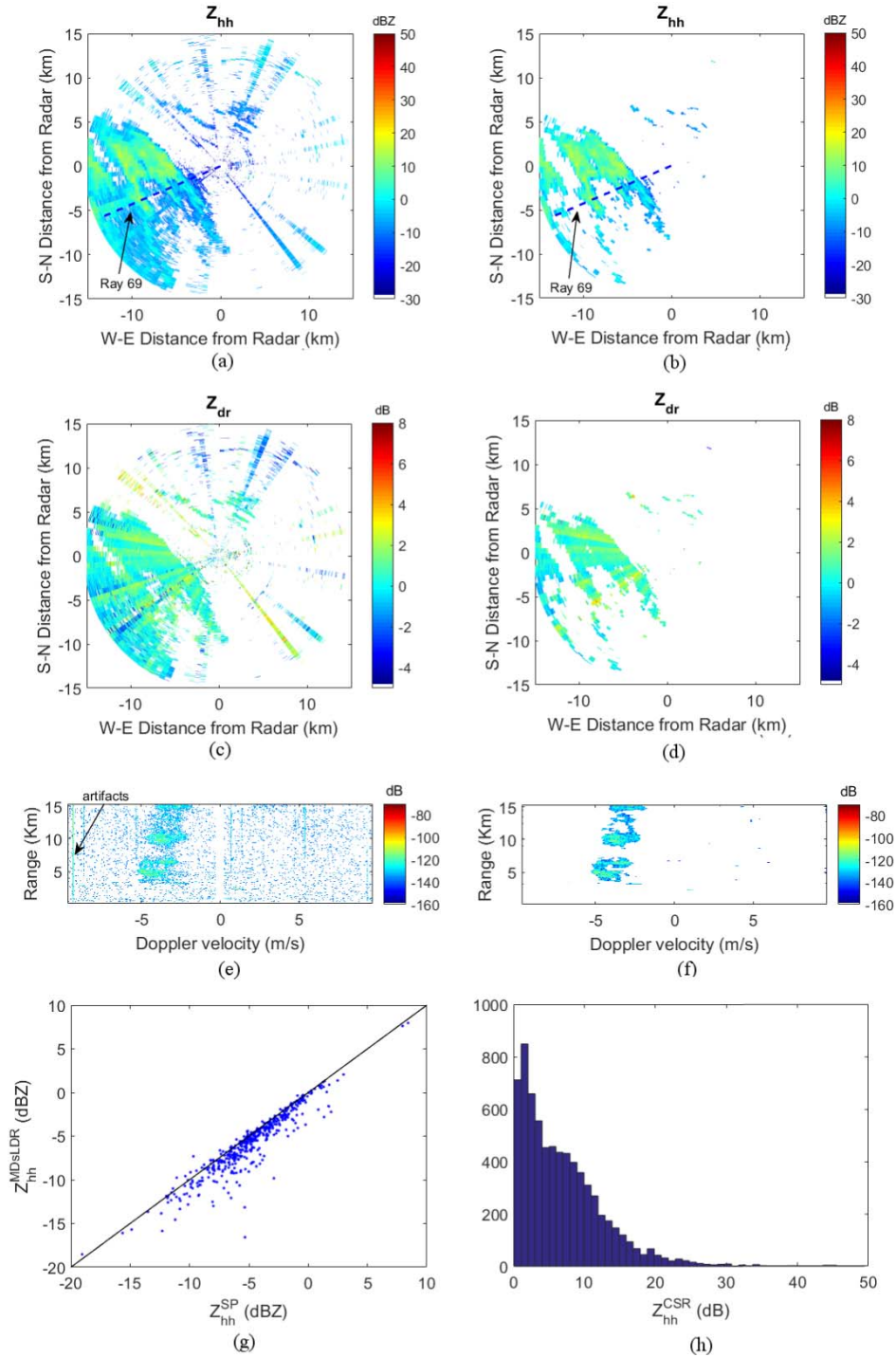


Fig. 9. Severe-artifacts case. Data measured at 12:00 UTC on January 15, 2016. (a) Z_{hh} after the standard processing. (b) Z_{hh} after the MDsLDR filter. (c) Z_{dr} after the standard processing. (d) Z_{dr} after the MDsLDR filter. (e) Spectrogram of Ray 69 after the standard processing. (f) Spectrogram of Ray 69 after the MDsLDR filter. (g) Z_{hh} comparison between the MDsLDR filter and the standard processing. (h) Clutter suppression ratio distribution.

artifacts. The reason behind this may be attributed to the security fence locating near the radar system. This speculation is based on the similar problem, which is well documented for the Meteo-France C-band polarimetric radar [37]. Further research should be conducted to improve the quality of the differential reflectivity.

The Ray 69 is extracted, and its corresponding range-Doppler spectrogram is further processed with the standard processing and the MDsLDR filter. The labeled artifacts

in Fig. 9(e) indicate the insufficient artifact mitigation for the standard processing. In this case, the artifacts have larger intensity than the weak precipitation. Compared with the standard processing, Fig. 9(f) shows that the MDsLDR filter suppresses more artifacts, ground clutter, and noise at the price of partial removal of a weak signal.

Finally, the scatter plot of the MDsLDR filtered Z_{hh} and the Z_{hh} after the standard processing is shown in Fig. 9(g). It shows that the reflectivity whose intrinsic values are less

than 0 dB is estimated smaller with the MDsLDR filter. This conclusion is consistent with the case in Fig. 6 and the reason behind this phenomenon is the good artifact mitigation performance of the newly proposed method. The histogram of the clutter suppression ratio is shown in Fig. 9(h). Note that the maximum clutter suppression ratio, in this case, is 49.5 dB.

VI. CONCLUSION

This paper proposes a new clutter suppression method named MDsLDR filter to remove the stationary and nonstationary narrow-band clutter in the spectral polarimetric radar. The MDsLDR filter relies on the Doppler spectral width and polarimetric properties of precipitation and clutter. This filter is mainly divided into four steps. First, a mask indicating the precipitation is obtained from the double sLDR filter. Second, a moving Doppler window is applied to the mask to further select precipitation. Third, a moving 2-D window is implemented to recover the removed precipitation and eliminate the remaining clutter. Finally, the mathematical morphology method is adopted to further reconstruct the precipitation area. The performance of the newly proposed method is verified qualitatively and quantitatively with the IDRA radar data, namely cases of moderate/light precipitation, storm with hook-echo signature and light precipitation with severe artifact contamination. The MDsLDR filter has clutter suppression ratio as high as 49.5 dB. Moreover, its effectiveness is verified for different Doppler velocity resolutions. This filter can remove the artifacts, the noise, and ground clutter, which are not overlapping with precipitation. For the case of the ground clutter mixed with precipitation, it should combine with another technique, such as the GMAP. The MDsLDR filter is also verified on the cases in the period from 2011 to 2016, and it shows robustness in artifacts, noise, and ground clutter suppression. Another advantage is that the MDsLDR filter is easy to implement, and it has relatively low computation complexity. Therefore the technique can be applied in real time. It is foreseeable that this new filter can mitigate other moving narrow-band clutter, such as airplanes, cars, and trains, in spectral polarimetric weather radar. More research can be done in this direction in the future.

ACKNOWLEDGMENT

J. Yin would like to thank the China Scholarship Council for supporting his study at the Delft University of Technology, The Netherlands. The authors would like to thank R. Reinoso-Rondinel for his discussion on the topic of clutter suppression.

REFERENCES

- [1] S. Fukao, K. Hamazu, and R. J. Doviak, *Radar for Meteorological and Atmospheric Observations*. Japan: Springer, 2014.
- [2] H. L. Groginsky and K. M. Glover, "Weather radar canceller design," in *Proc. 19th Conf. Radar Meteorol.*, vol. 1, 1980, pp. 192–198.
- [3] A. Siggia and R. Passarelli, "Gaussian model adaptive processing (GMAP) for improved ground clutter cancellation and moment calculation," in *Proc. ERAD*, vol. 2, 2004, pp. 421–424.
- [4] J. Hubbert, M. Dixon, and S. Ellis, "Weather radar ground clutter. Part II: Real-time identification and filtering," *J. Atmos. Ocean. Technol.*, vol. 26, no. 7, pp. 1181–1197, 2009.
- [5] J. Hubbert, M. Dixon, S. Ellis, and G. Meymaris, "Weather radar ground clutter. Part I: Identification, modeling, and simulation," *J. Atmos. Ocean. Technol.*, vol. 26, no. 7, pp. 1165–1180, 2009.
- [6] R. L. Ice *et al.*, "Automatic clutter mitigation in the WSR-88D, design, evaluation, and implementation," in *Proc. 34th Conf. Radar Meteorol.*, Williamsburg, VA, USA, 2009.
- [7] Y. Li, G. Zhang, R. J. Doviak, L. Lei, and Q. Cao, "A new approach to detect ground clutter mixed with weather signals," *IEEE Trans. Geosci. Remote Sens.*, vol. 51, no. 4, pp. 2373–2387, Apr. 2013.
- [8] Q. Cao, G. Zhang, R. D. Palmer, M. Knight, R. May, and R. J. Stafford, "Spectrum-time estimation and processing (STEP) for improving weather radar data quality," *IEEE Trans. Geosci. Remote Sens.*, vol. 50, no. 11, pp. 4670–4683, Nov. 2012.
- [9] D. A. Warde and S. M. Torres, "The autocorrelation spectral density for doppler-weather-radar signal analysis," *IEEE Trans. Geosci. Remote Sens.*, vol. 52, no. 1, pp. 508–518, Jan. 2014.
- [10] S. Torres, D. Warde, and D. Zrníc, "Signal design and processing techniques for WSR-88D ambiguity resolution: Part 15 the CLEAN-AP filter," Nat. Severe Storms Lab., Norman, OK, USA, Tech. Rep., 2012.
- [11] H. Liu and V. Chandrasekar, "Classification of hydrometeors based on polarimetric radar measurements: Development of fuzzy logic and neuro-fuzzy systems, and *in situ* verification," *J. Atmos. Ocean. Technol.*, vol. 17, no. 2, pp. 140–164, 2000.
- [12] H. S. Park, A. Ryzhkov, D. Zrníc, and K.-E. Kim, "The hydrometeor classification algorithm for the polarimetric WSR-88D: Description and application to an MCS," *Weather Forecasting*, vol. 24, no. 3, pp. 730–748, 2009.
- [13] V. N. Mahale, G. Zhang, and M. Xue, "Fuzzy logic classification of S-band polarimetric radar echoes to identify three-body scattering and improve data quality," *J. Appl. Meteorol. Climatol.*, vol. 53, no. 8, pp. 2017–2033, 2014.
- [14] D. N. Moisseev and V. Chandrasekar, "Polarimetric spectral filter for adaptive clutter and noise suppression," *J. Atmos. Ocean. Technol.*, vol. 26, no. 2, pp. 215–228, 2009.
- [15] B.-Y. Ye, G. Lee, and H.-M. Park, "Identification and removal of non-meteorological echoes in dual-polarization radar data based on a fuzzy logic algorithm," *Adv. Atmos. Sci.*, vol. 32, no. 9, pp. 1217–1230, 2015.
- [16] P. M. Stepanian and K. G. Horton, "Extracting migrant flight orientation profiles using polarimetric radar," *IEEE Trans. Geosci. Remote Sens.*, vol. 53, no. 12, pp. 6518–6528, Dec. 2015.
- [17] D. S. Zrníc and A. V. Ryzhkov, "Observations of insects and birds with a polarimetric radar," *IEEE Trans. Geosci. Remote Sens.*, vol. 36, no. 2, pp. 661–668, Mar. 1998.
- [18] V. Melnikov, M. Leskinen, and J. Koistinen, "Doppler velocities at orthogonal polarizations in radar echoes from insects and birds," *IEEE Geosci. Remote Sens. Lett.*, vol. 11, no. 3, pp. 592–596, Mar. 2014.
- [19] V. M. Melnikov, M. J. Istok, and J. K. Westbrook, "Asymmetric radar echo patterns from insects," *J. Atmos. Ocean. Technol.*, vol. 32, no. 4, pp. 659–674, 2015.
- [20] L. Alku, D. Moisseev, T. Aittomäki, and V. Chandrasekar, "Identification and suppression of nonmeteorological echoes using spectral polarimetric processing," *IEEE Trans. Geosci. Remote Sens.*, vol. 53, no. 7, pp. 3628–3638, Jul. 2015.
- [21] O. A. Krasnov and A. G. Yarovoy, "Polarimetric micro-Doppler characterization of wind turbines," in *Proc. 10th Eur. Conf. Antennas Propag. (EuCAP)*, Apr. 2016, pp. 1–5.
- [22] A. Huuskonen, E. Saltikoff, and I. Holleman, "The operational weather radar network in Europe," *Bull. Amer. Meteorol. Soc.*, vol. 95, no. 6, pp. 897–907, 2014.
- [23] P. Joe, J. Scott, J. Sydor, A. Brandão, and A. Yongacoglu, "Radio local area network (RLAN) and C-band weather radar interference studies," in *Proc. 32nd Conf. Radar Meteorol.*, 2005.
- [24] E. Saltikoff *et al.*, "The threat to weather radars by wireless technology," *Bull. Amer. Meteorol. Soc.*, vol. 97, no. 7, pp. 1159–1167, 2016.
- [25] L. Najman and H. Talbot, *Mathematical Morphology*. Hoboken, NJ, USA: Wiley, 2013.
- [26] J. I. Figueras Ventura, "Design of a high resolution X-band Doppler polarimetric radar," Ph.D. dissertation, Dept. Geosci. Remote Sens., Delft Univ. Technol., Delft, The Netherlands, 2009.
- [27] T. Otto and H. W. Russchenberg, "High-resolution polarimetric X-band weather radar observations at the Cabauw Experimental Site for Atmospheric Research," *Geosci. Data J.*, vol. 1, no. 1, pp. 7–12, 2014.
- [28] (Apr. 2017). *IDRA Data Website*. [Online]. Available: <http://data.4tu.nl/repository/collection:cabauw>

- [29] C. Unal, "Spectral polarimetric radar clutter suppression to enhance atmospheric echoes," *J. Atmos. Ocean. Technol.*, vol. 26, no. 9, pp. 1781–1797, 2009.
- [30] F. Yanovsky, "Inferring microstructure and turbulence properties in rain through observations and simulations of signal spectra measured with Doppler–polarimetric radars," in *Proc. Polarimetric Detection, Characterization Remote Sens.*, 2011, pp. 501–542.
- [31] F. J. Yanovsky, "Spectral-polarimetric method of objects and phenomena observation," in *Proc. 5th World Congr. Aviation 21st Century*, vol. 2, 2012, pp. 3–7.
- [32] R. J. Doviak and D. S. Zrnic, *Doppler Radar and Weather Observations*. Orlando, FL, USA: Academic, 2014.
- [33] M. Hagen and P. Meischner, "Estimation of rainfall parameters from polarimetric radar measurements with POLDIRAD," *Phys. Chem. Earth, B, Hydrol., Oceans Atmos.*, vol. 25, no. 10, pp. 849–853, 2000.
- [34] L. Li, G. M. Heymsfield, P. E. Racette, L. Tian, and E. Zenker, "A 94-GHz cloud radar system on a NASA high-altitude ER-2 aircraft," *J. Atmos. Ocean. Technol.*, vol. 21, no. 9, pp. 1378–1388, 2004.
- [35] K. Sato and H. Okamoto, "Characterization of Z_e and LDR of non-spherical and inhomogeneous ice particles for 95-GHz cloud radar: Its implication to microphysical retrievals," *J. Geophys. Res. Atmos.*, vol. 111, no. D22213, 2006.
- [36] R. M. Beauchamp and V. Chandrasekar, "Robust linear depolarization ratio estimation for dual-polarization weather radar," *IEEE Trans. Geosci. Remote Sens.*, vol. 54, no. 3, pp. 1462–1474, Apr. 2016.
- [37] J. J. Gourley, P. Tabary, and J. P. du Chatelet, "Data quality of the Meteo–France C-band polarimetric radar," *J. Atmos. Ocean. Technol.*, vol. 23, no. 10, pp. 1340–1356, 2006.



Jiapeng Yin (S'16) received the B.S. degree in information engineering from the National University of Defense Technology, Changsha, China, in 2012. He is currently pursuing the Ph.D. degree with the Group of Atmospheric Remote Sensing, Delft University of Technology, Delft, The Netherlands.

His research interests include weather radar clutter suppression and weather radar calibration.



Christine M. H. Unal received the master's degree in physics from the University of Nice Sophia Antipolis, Nice, France, in 1986, and the D.E.A. degree in physics for remote sensing from the University of Paris, Paris, France, in 1987.

She joined the Delft University of Technology, Delft, The Netherlands, in 1988, where she was with the International Research Center for Telecommunications and Radar. Since 2012, she has been with the Department of Geoscience and Remote Sensing and the Delft Climate Institute, Delft University of Technology. She was involved in radar polarimetric calibration and radar spectral polarimetry (quasi-simultaneous Doppler spectra of polarimetric measurements and their processing and interpretation). Since 2003, she has been applying this expertise to enhance the processing of atmospheric echoes. She is currently a Research Scientist with the Delft University of Technology. Her research interests include weather/atmospheric radar signal processing and searching for new retrieval techniques to estimate the microphysical and dynamical properties of precipitation using ground-based radars.



Herman W. J. Russchenberg is currently the Director of the TU Delft Climate Institute and the Head of the Department of Geoscience and Remote Sensing. He is also a Specialist in remote sensing of clouds and precipitation with ground-based radar, lidar, and microwave radiometry. He is experienced in the theoretical and experimental research of the scattering process and the retrieval of geophysical parameters from radar and lidar measurements. He is one of the leading scientists of the Cabauw Experimental Site for Atmospheric Research.